Editors' Suggestion

Local phase shift due to interactions in an atom interferometer

Zhibin Yao,[1] Cyrille Solaro,[1] Corentin Carrez,[1] Pierre Cladé,[1] and Saïda Guellati-Khelifa[1,2,*]

[1]*Laboratoire Kastler Brossel, Sorbonne Université, CNRS, ENS-PSL, Collège de France, 4 place Jussieu, 75005 Paris, France*

[2]*Conservatoire National des Arts et Métiers, 292 rue Saint Martin, 75003 Paris, France*

(Received 11 July 2022; accepted 22 September 2022; published 14 October 2022)

We study the phase shift induced by atomic interactions at the output of an atom interferometer. Due to the mutual interaction between the two overlapping Bose-Einstein condensates, the phase exhibits a spatial profile. We evaluate the phase gradient using a perturbative method based on the Feynman path-integral approach. Our model accounts for the effects of the population imbalance between the two arms of the interferometer and the difference between the scattering lengths of the hyperfine levels. We also investigate these effects experimentally by measuring the interaction phase shift for a set parameters. Our experimental results are well reproduced by our theoretical model.

DOI: 10.1103/PhysRevA.106.043312

I. INTRODUCTION

Matter-wave interferometry has been used to measure with extreme accuracy several physical quantities [1] such as gravity [2–7], inertial forces [8–11], and fundamental constants [12–14] enabling advanced tests of general relativity [15–18] and quantum electrodynamics [13,14]. In addition, many experiments based on atom interferometry are underway or have been proposed in order to test short-range forces [19–22] and different models of particle physics in the search for unknown forces or dark energy [23–29]. This technology, which has not yet reached its full potential, is also at the heart of large-scale or space instruments [30–32]. These instruments are being built, with targeted significantly improved performances, for testing fundamental physics with unprecedented accuracy, detecting gravitational waves [33–36], and mapping the Earth's gravitational field from satellites [37,38].

Both the sensitivity and accuracy of the most advanced atom interferometers are limited by the transverse motion of the atomic cloud [39], which exalts systematic effects related to short-scale intensity fluctuations [40], the Gouy phase, and wave-front curvature [41]. Due to wave-front distortions, transverse motion also limits the diffraction order of large-momentum beam splitters [42–45]. In this context, Bose-Einstein condensates (BECs) constitute ideal atomic sources. In addition, the atomic interactions that are inherent in such dense clouds can generate spin squeezing, which could be exploited to surpass the standard quantum limit [46–48].

However, atomic interactions also induce a detrimental phase shift that can undermine the benefits of using Bose-Einstein condensates for precision measurements with atom interferometry. Effects of interactions have been studied both theoretically and experimentally to understand their impact on the phase of Bose-Einstein condensates during free evolution [49–53]. Early work showed that upon release from the trapping potential, the BEC expands due to repulsive interactions and develops a nonuniform phase profile [54–56]. In Ref. [49], the authors measured the functional form and time evolution of this phase profile by combining interferometry with spatially resolved autocorrelation. They also measured the small velocity imparted to the two BEC wave packets from their mutual repulsion. More recent work has focused on the local modification of the condensate phase due to mutual interactions and has showed that modifications occur only in the region where the wave packets overlap [53].

This nonuniform phase profile impacts the accuracy of measurements based on atom interferometry. In this paper, we experimentally evaluate this effect by measuring locally the phase shift at the output port of an atom interferometer and its dependence upon the population imbalance, the trapping-potential frequencies, and the condensate release time. Furthermore, we present an approach to calculate the effect of interactions using the Feynman path integral. Numerical simulation based on this method reproduces well our experimental data. This approach differs from that used in previous works [50–53] where the evolution of the BEC phase was obtained from the Gross-Pitaevskii equation by considering the time evolution of its density. In most works the expansion of the condensate is described by the Castin-Dum model [57] valid in the Thomas-Fermi regime. Our method based on the Feynman path integral allows us to calculate the phase shift at the output of the interferometer for any geometry. It also allows the contributions of the self- and mutual interactions to be evaluated separately.

This paper is organized as follows. Section II presents the theoretical model we have developed to evaluate the phase shift at the output of an atomic interferometer formed by a sequence of three light pulses in the so-called Mach-Zehnder configuration (see Fig. 1). Each pulse induces a stimulated Raman transition. We use a perturbation approach to derive a general formula for calculating the effects of self-interaction and mutual interaction between the two interfering condensates. Finally, based on Castin and Dum's description of the BEC wave function, we obtain a formula for the phase profile, the signature of the mutual interaction. In Sec. III we present a

*guellati@lkb.upmc.fr

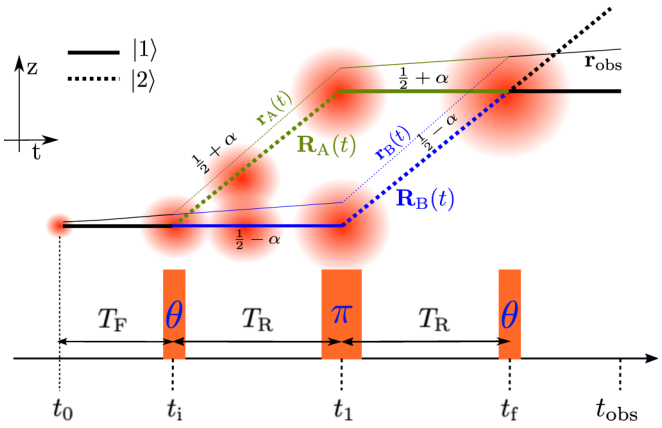

FIG. 1. At time t_0 we release the BEC from the dipole optical trap. During the free-fall time, it expands, and the interaction energy decreases. After a falling time T_F, we apply the three-pulse sequence θ-π-θ. Trajectory A is in green, and trajectory B is in blue. Solid lines show state $|1\rangle$, and dashed lines show state $|2\rangle$. Thick lines show the trajectories $R_{A/B}$ of the center of mass of the atomic wave packet. Thin lines show the trajectory $r_{A/B}$ used to integrate the Lagrangian for a given final position $\boldsymbol{r}_{\rm obs}$

set of experimental results. We study the behavior of both the phase gradient and the total interaction phase shift by varying different experimental parameters.

II. THEORETICAL EVALUATION OF THE INTERACTION PHASE SHIFT

The goal of this section is to calculate the phase at the output of an atom interferometer in the mean-field approximation using the Feynman path-integral method [58]. Here, we apply this approach, which is commonly used in atom interferometry to calculate the phase induced by the external potential, to the case of the mean field. The Feynman path-integral method states that, given an initial wave packet with phase $\phi(\boldsymbol{r}(t_0), t_0)$ at time t_0, the phase at time t can be calculated by integrating the Lagrangian $\mathcal{L}$ along the classical trajectory $\boldsymbol{r}(t)$ that makes the action extremal:

$$\phi(\boldsymbol{r}(t), t) - \phi(\boldsymbol{r}(t_0), t_0) = \frac{1}{\hbar}\int_{t_0}^{t} \mathcal{L}(\dot{\boldsymbol{r}}(t), \boldsymbol{r}(t), t)dt, \qquad (1)$$

with

$$\mathcal{L}(\dot{\mathbf{r}}(t), \mathbf{r}(t), t) = \tfrac{1}{2}m\dot{\mathbf{r}}^2(t) - V(\mathbf{r}, t) \qquad (2)$$

and V being the potential experienced by an atom of mass m. The trajectory should match the initial velocity of the cloud $[\dot{\boldsymbol{r}}(t_0) = -i(\hbar\nabla\phi/m)]$.

In the mean-field approximation, the interaction potential is proportional to the cloud density $\rho(\boldsymbol{r}, t)$. To calculate the phase in our interferometer, we have to consider the internal states and the effect of the Raman transition. The Raman transition couples two internal states, namely, $|1\rangle$ and $|2\rangle$. The total mean field experienced by an atom in state $|i\rangle$ is the sum of the mean field induced by the atoms in state $|i\rangle$ from its own atomic cloud (the so-called self-interaction) and the one induced by the atoms from the other cloud (the so-called mutual interaction; see Fig. 1). It can be written as

$$V_{\rm MF}(\boldsymbol{r}, t, i) = \sum_j N g_{ij}\rho(\boldsymbol{r}, t, j), \qquad (3)$$

with $g_{ij} = 4\pi\hbar^2 a_{ij}/m$, where a_{ij} are the scattering lengths. The interaction potential depends on the normalized density $\rho(\boldsymbol{r}, t, j)$ of the atoms in the internal states $|j\rangle$.

Raman transitions are performed with two counterpropagating laser beams ($\boldsymbol{k}_1, \omega_1$ and $\boldsymbol{k}_2, \omega_2$), leading to an effective momentum $\boldsymbol{k}_{\rm eff} = \boldsymbol{k}_1 - \boldsymbol{k}_2$ and pulsation $\omega = \omega_1 - \omega_2$ [59]. To use the Lagrangian formalism, one can take into account the effect of the Raman transitions with an effective potential. For the three-pulse interferometer in Fig. 1, this potential is given for each path A and B by [60]

$$W_A(\boldsymbol{r}, t) = \hbar[\boldsymbol{k}_{\rm eff}\cdot\boldsymbol{r}(t) - \omega t][\delta(t - t_i) - \delta(t - t_1)], \qquad (4)$$

$$W_B(\boldsymbol{r}, t) = \hbar[\boldsymbol{k}_{\rm eff}\cdot\boldsymbol{r}(t) - \omega t][\delta(t - t_1) - \delta(t - t_{\rm f})]. \qquad (5)$$

Indeed, when an atom performs a Raman transition and is transferred from $|1\rangle$ to $|2\rangle$, the effective phase of the laser is added to the phase of its wave function. It is subtracted when the atom is transferred from state $|2\rangle$ to state $|1\rangle$. With this effective potential, the trajectory that extremizes the action accounts for the recoil induced by each Raman transition.

To compute the phase difference at a given observation position $\boldsymbol{r}_{\rm obs}$ and time $t_{\rm obs}$ (see Fig. 1), we consider two trajectories, $\boldsymbol{r}_A(t)$ and $\boldsymbol{r}_B(t)$, which start with the initial velocity $\boldsymbol{v}_0$ of the cloud and satisfy $\boldsymbol{r}_A(t_{\rm obs}) = \boldsymbol{r}_B(t_{\rm obs}) = \boldsymbol{r}_{\rm obs}$ (note that they may not start at the same position). The spatially dependent phase difference between the two waves is given by

$$\Delta\phi(\boldsymbol{r}_{\rm obs}) = \phi(\boldsymbol{r}_A(t_0), t_0) - \phi(\boldsymbol{r}_B(t_0), t_0) + \frac{1}{\hbar}\int_{t_0}^{t_{\rm obs}} [\mathcal{L}_A(\dot{\boldsymbol{r}}_A, \boldsymbol{r}_A, t) - \mathcal{L}_B(\dot{\boldsymbol{r}}_B, \boldsymbol{r}_B, t)]dt. \qquad (6)$$

In typical experiments, the Thomas-Fermi approximation is applicable, and the Castin-Dum description of the BEC density [57] is commonly used. However, due to the mutual interaction, it is not possible to compute analytically the density in each branch of the interferometer and therefore the classical trajectories which depend on the interaction potential. We propose here to treat the mutual interaction as a perturbation.

Let us now consider a reference configuration in which (i) there is no interaction between the two clouds and (ii) the mean field is the same on both arms of the interferometer (same scattering length $g_{11} = g_{22}$ and a 50:50 atomic beam splitter). In this situation, the two clouds are identical with respect to their centers of mass and have the same density $\rho_{\rm ref}(\boldsymbol{r}, t)$. The reference potential used to calculate the classical trajectories is

$$V_{{\rm ref},A/B}(\boldsymbol{R}_{A/B}(t) + \boldsymbol{r}, t) = c_{\rm ref}(t) N g_{11}\rho_{\rm ref}(\boldsymbol{r}, t), \qquad (7)$$

where $\boldsymbol{R}_{A/B}$ are the trajectories of the centers of mass (thick lines in Fig. 1) and

$$c_{\rm ref}(t) = \begin{cases} 1 & t < t_i, \\ \frac{1}{2} & t_i \leqslant t \leqslant t_{\rm obs}. \end{cases} \qquad (8)$$

Assuming that the shape of the cloud is given by this reference density, the potential due to the atomic interactions felt by the atoms in the cloud along trajectory A, for $t_i < t < t_f$, is

$$V_A(\boldsymbol{R}_A(t)+\boldsymbol{r},t) = N\frac{g_{11}}{2}\rho_{\rm ref}(\boldsymbol{r},t) + N\left[c_A(t)g_{\xi_A(t),\xi_A(t)} - \frac{g_{11}}{2}\right]\rho_{\rm ref}(\boldsymbol{r},t) + Nc_B(t)g_{\xi_A(t),\xi_B(t)}\rho_{\rm ref}(\boldsymbol{r}+\Delta\boldsymbol{R},t), \quad (9)$$

where $\xi_{A/B}(t)$ represents the internal state of the atom (1 or 2), $c_{A/B}(t)$ is the proportion of atoms in path A or B, and $\Delta\boldsymbol{R}(t) = \boldsymbol{R}_A(t) - \boldsymbol{R}_B(t)$. The first term corresponds to the reference potential, the second corresponds to the correction of the self-interaction due to the difference in the scattering lengths a_{11} and a_{22}, and the last term corresponds to the mutual interaction. For trajectory B, there is a similar equation, exchanging A and B and replacing $\Delta\boldsymbol{R}(t)$ by $-\Delta\boldsymbol{R}(t)$.

For rubidium, $|(a_{22}-a_{11})/a_{11}|$ is around 6%, and in a typical experiment, the population imbalance is a few percent. Moreover, the mutual interaction term is non-negligible only when the two clouds overlap. Our approximation consists of considering the last two terms of Eq. (9) as perturbations when we derive the equations of motion for the classical trajectories. This means that only the first term of Eq. (9) is responsible for the repulsive force. We denote by $V^{\rm pert}_{\rm A/B}$ the interaction potential that accounts for the last two terms.

We now consider an atom after the first Raman pulse. It is in a superposition of two wave packets that propagate along the reference trajectories $\boldsymbol{r}_A$ and $\boldsymbol{r}_B$. These trajectories are determined from the reference configuration. Due to symmetry, the relative trajectories with respect to the motion of the center of mass are the same: we can write $\boldsymbol{r}_{A/B}(t) = \boldsymbol{R}_{A/B}(t) + \boldsymbol{r}_{\rm ref}(t)$. In the absence of any perturbation, the two trajectories are symmetric, and the total phase shift at the output of the interferometer is zero. At first order, the total phase shift could be calculated by integrating the perturbation along the unperturbed trajectories [58]. These trajectories overlap for $t < t_i$ and $t > t_f$, and the potential is the same (atoms are in the same state); we can therefore restrict the integral to $t_i < t < t_f$ and

$$\Delta\phi(\boldsymbol{r}_{\rm obs}) = \frac{1}{\hbar}\int_{t_i}^{t_f}\left[V_A^{\rm pert}(\boldsymbol{R}_A(t)+\boldsymbol{r}_{\rm ref}(t),t) - V_B^{\rm pert}(\boldsymbol{R}_B(t)+\boldsymbol{r}_{\rm ref}(t),t)\right]dt. \quad (10)$$

By separating contributions from mutual and self-interaction, we obtain

$$\Delta\Phi^{\rm self}(\boldsymbol{r}_{\rm obs}) = \frac{1}{\hbar}N\alpha(g_{11}+g_{22})\int_{t_{\rm i}}^{t_{\rm f}}\rho_{\rm ref}(\boldsymbol{r},t)\,dt + \frac{1}{\hbar}\frac{N}{2}\delta g\left[\int_{t_{\rm i}}^{t_1}\rho_{\rm ref}(\boldsymbol{r},t)\,dt - \int_{t_1}^{t_{\rm f}}\rho_{\rm ref}(\boldsymbol{r},t)\,dt\right], \quad (11)$$

$$\Delta\Phi^{\rm mut}(\boldsymbol{r}_{\rm obs}) = \frac{1}{\hbar}Ng_{21}\left(\frac{1}{2}-\alpha\right)\left[\int_{t_{\rm i}}^{t_{\rm s}^A}\rho_{\rm ref}(\boldsymbol{r}+\Delta\boldsymbol{R}(t),t)\,dt + \int_{t_{\rm c}^A}^{t_{\rm f}}\rho_{\rm ref}(\boldsymbol{r}+\Delta\boldsymbol{R}(t),t)\,dt\right] - \frac{1}{\hbar}Ng_{12}\left(\frac{1}{2}+\alpha\right)\left[\int_{t_{\rm i}}^{t_{\rm s}^B}\rho_{\rm ref}(\boldsymbol{r}-\Delta\boldsymbol{R}(t),t)\,dt + \int_{t_{\rm c}^B}^{t_{\rm f}}\rho_{\rm ref}(\boldsymbol{r}-\Delta\boldsymbol{R}(t),t)\,dt\right], \quad (12)$$

where $\alpha = |c_A(t) - c_B(t)|/2$ is the population imbalance between the two arms of the interferometer and $\delta g = g_{22} - g_{11}$. The boundaries of the integrals (11) and (12) account for the finite extension of the two interfering clouds: $t_{\rm s}^A$ ($t_{\rm s}^B$) is the separation time when the atom on trajectory A (B) leaves the overlap zone, and $t_{\rm c}^A$ ($t_{\rm c}^B$) is the recombination time when the atom on trajectory A (B) enters the overlap zone. They depend on the expansion and the separation velocities of the two interfering condensates.

The Castin-Dum model [57] provides a good description of the BEC dynamics in time-dependent traps when the Thomas-Fermi approximation is satisfied. It gives the following formula for the BEC density at time t:

$$\rho(\mathbf{r},t) = \frac{\mu}{g_{11}\lambda_x(t)\lambda_y(t)\lambda_z(t)}\times\left(1-\sum_{s=x,y,z}[r_s(t)/r_{s1}\lambda_s(t)]^2\right) \quad (13)$$

when the last term is positive and $\rho(\mathbf{r},t) = 0$ otherwise. μ denotes the chemical potential of the initial state, i.e., of the system before the application of the first Raman light pulse:

$$\mu = \frac{\hbar\bar{\omega}}{2}\left(15Na\sqrt{\frac{m\bar{\omega}}{\hbar}}\right)^{\frac{2}{5}}, \quad \bar{\omega} = (\omega_x\omega_y\omega_z)^{\frac{1}{3}}. \quad (14)$$

ω_s is the optical trap frequency along the s axis, $r_{s1} = \sqrt{2\mu/m\omega_s^2}$ is the Thomas-Fermi radius, and the scaling factor $\lambda_s(t)$ is governed by differential equations derived by Castin and Dum from the scaling ansatz for a single-component BEC [57]:

$$\frac{d^2\lambda_s(t)}{dt^2} = \frac{\omega_s^2}{\lambda_s(t)\lambda_x(t)\lambda_y(t)\lambda_z(t)}. \quad (15)$$

In our experiment, the Raman beams propagate along the z axis. The two clouds hence separate along this direction, leading to a phase gradient from the mutual interaction. We obtain the spatial profile of the phase shift $\Delta\Phi^{\rm mut}(z)$ by averaging Eq. (12) over transverse coordinates (x, y).

For $\alpha = 0$ (perfect $\pi/2$ Raman pulses), we show that the phase $\Delta\Phi^{\rm mut}$ can be written in first order in z as

$$\Delta\Phi^{\rm mut}(z_{\rm obs}) = \frac{2}{\hbar}\frac{a_{12}}{2a_{11}}\frac{z_{\rm obs}}{\lambda_z(t_{\rm obs})}\int_{t_{\rm i}}^{t_{\rm f}}\mu(t)f(\Delta Z_{\rm R})dt, \quad (16)$$

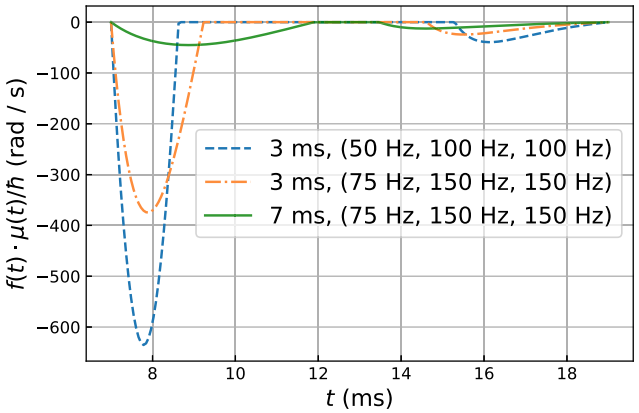

FIG. 2. Evolution of the quantity $f(\Delta Z_R)\mu(t)$ during the interferometer sequence for different values of the release time T_F and trapping frequencies.

with

$$\mu(t) = \frac{\mu}{\lambda_x(t)\lambda_y(t)\lambda_z(t)}, \quad \Delta Z_R = \frac{\Delta Z}{z_l \lambda_z(t)}, \tag{17}$$

and the function f is defined by

$$f(x) = \begin{cases} x(x^4 - 1) & \text{if } x < 1, \\ 0 & \text{otherwise.} \end{cases} \tag{18}$$

The form of Eq. (16) is interesting as it dissociates the effects of the chemical potential $\mu(t)$ and of the separation of the two condensates $f(\Delta Z_R)$. The temporal evolution of these two terms depends on the expansion dynamics of the condensate, which is set by the trap frequencies. In Fig. 2 we plot $\mu(t)f(\Delta Z_R)$ for two sets of trapping frequencies and two different release times T_F. We clearly observe that the mutual interaction is significant at the beginning of the interferometer and that it decreases as the condensates dilute.

III. EXPERIMENT

We produce a ^{87}Rb Bose-Einstein condensate by evaporative cooling in an all-optical trap which consists of three Gaussian laser beams at a wavelength of 1070 nm. Two relatively wide beams of 170-μm waist cross under a shallow angle and provide a large trapping volume, the so-called *reservoir*, which is loaded from an optical molasses. A tightly focused third beam of 25-μm waist, the so-called *dimple beam*, crosses the reservoir at an angle of 65°. This geometry provides the high confinement necessary for efficient evaporation. The maximum laser power in the reservoir and in the dimple is 24 and 0.5 W, respectively. To produce a BEC in a pure Zeeman state, we use the spin-distillation technique [61], where we apply a magnetic field gradient during evaporation that selectively reduces the depth of the trap for magnetically sensitive states. We produce about 220 000 atoms in $|F = 1, m_F = 0\rangle$ after 1.7 s of evaporation. The trapping frequencies (ν_x, ν_y, ν_z) at the end of the evaporation were measured to be (50(2), 115(10), 115(10)) Hz. At time t_0, the BEC is released by turning off the trapping potential and falls freely for a duration T_F prior to us applying the light-pulse sequence θ-π-θ (Fig. 1). Each light pulse consists of two vertically counterpropagating laser beams, which drive Raman transitions between the two hyperfine levels $|F = 1, m_F = 0\rangle$ (state $|1\rangle$) and $|F = 2, m_F = 0\rangle$ (state $|2\rangle$) of the $5S_{1/2}$ electronic ground state. The two Raman lasers are phase locked. A detailed description of the electronic system for controlling their frequencies and their phase difference is given in the supplementary material of Ref. [14]. The first light pulse splits the initial Bose-Einstein condensate into two wave packets. The relative atom number between the two arms (i.e., the parameter α) is controlled by adjusting the duration of the first light pulse. Figure 3 gives an overview of the experimental setup. To measure the number of atoms in $F = 2$ and $F = 1$, we use a sequence of three probe laser pulses, each resonant with the cycling transition ($^5S_{1/2}\, F = 2 \longrightarrow {}^5P_{3/2}\, F' = 3$). The first pulse measures the number of atoms in $F = 2$, which are then pushed away (pusher beam). The atoms in $F = 1$ are first pumped to $F = 2$, then detected by the second probe pulse. The third pulse shines on the camera without atoms to get a reference picture of the laser beam intensity.

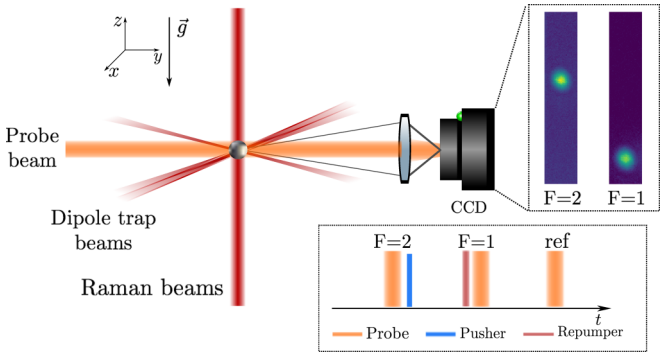

FIG. 3. An overview of the experimental setup. The bottom inset shows the detection timing sequence.

To probe the atomic phase, we scan the phase difference of the Raman lasers $\Delta\phi_L$ at the third light pulse. We measure by absorption imaging and for different values of $\Delta\phi_L$ the number of atoms in each of the two hyperfine states $F = 1$ and $F = 2$ at the end of the interferometer sequence. The top of Fig. 4 shows the absorption images (yz plane) of the atomic cloud in $F = 1$ taken 33 ms after release from the trap for a set of $\Delta\phi_L$ values. We clearly observe a shift in the center position of the imaged cloud which reveals that the phase is not spatially uniform. To obtain the phase at the z position, we integrate the two-dimensional absorption image, along the y dimension. Then, for each position z, which corresponds to a camera pixel, we calculate the number of atoms as a function of the laser phase $\Delta\Phi_L$ and fit those data with a cosine function to extract the atomic phase. This phase is plotted in the bottom of Fig. 4 for different values of the pulse area θ. For $\theta = \pi/2$, we measure a phase gradient of 3.6 mrad/μm after a fall time of 7 ms for a BEC with an initial atomic density of 4.3×10^{14} atoms/cm^3. The simulation based on our model fits the experimental data without any adjustment. These theoretical curves were obtained as follows: we first consider an atom at an initial position $\mathbf{r}(t_0)$ and calculate, for all times t between t_0 and t_{obs}, the expansion parameters $\lambda_s(t)$ by numerically solving Eq. (15) and, subsequently, the coordinates $r_s(t) = r_s(0)\lambda_s(t)$ $(s = x, y, z)$. We then determine the

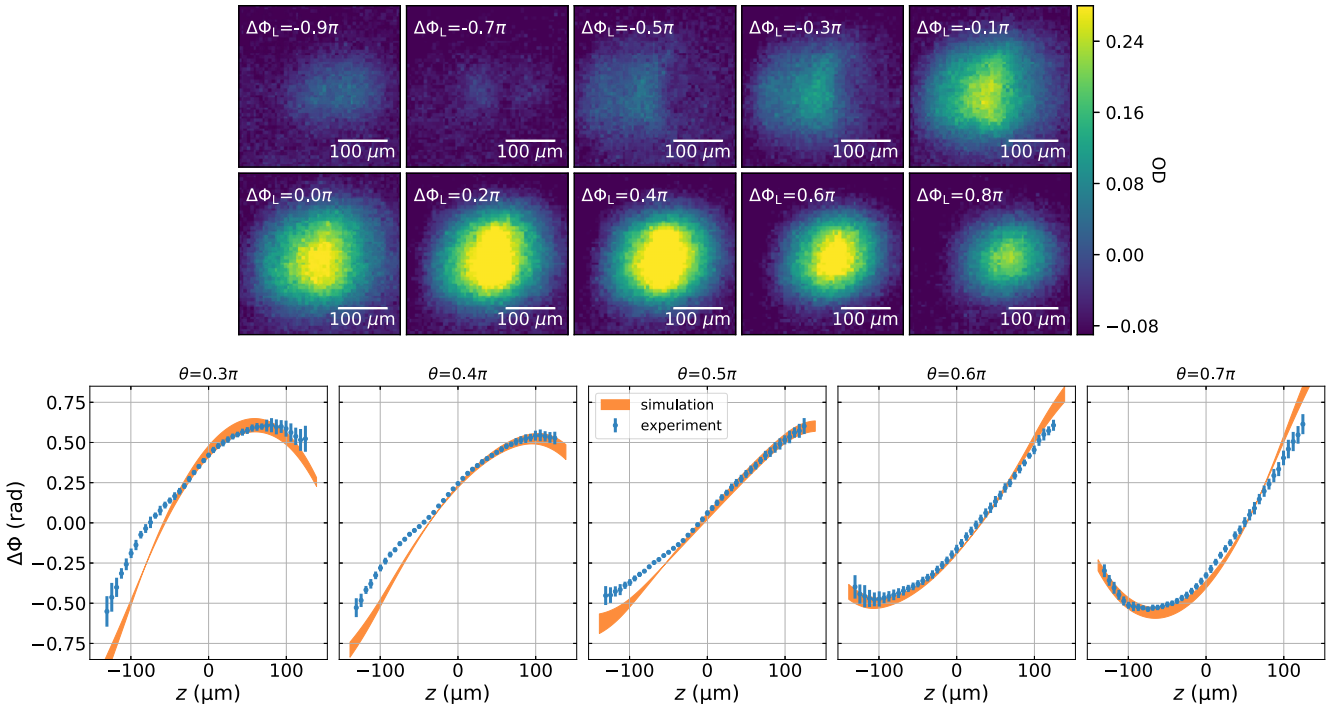

FIG. 4. Top: Absorption pictures obtained by scanning the phase difference $\Delta\Phi_L$ between the two Raman lasers at the last pulse from $-\pi$ to π. Optical densities greater than 0.25 have been saturated. The experimental parameters are $T_R = 6$ ms, $T_F = 7$ ms, and $\theta = 0.3\pi$. Bottom: Variation of the phase shift at the output of the interferometer along the vertical z axis for different Raman pulse areas θ. The shaded area accounts for the fluctuation of the pulse area and trapping frequencies.

reference trajectories A and B that account for the effect of the Raman transitions. Finally, we calculate the accumulated phase shift $\Delta\Phi_{at}$ using Eqs. (11) and (12).

At time t after the overlap of the wave packets, the probability $P(F = 1)$ of detecting the atom in $|F = 1\rangle$ at position $\boldsymbol{r}$ is

$$P(F{=}1){=}\frac{\mu - \frac{1}{2}\sum m\omega_s^2 r_s^2(0)}{g_{11}N\lambda_x(t)\lambda_y(t)\lambda_z(t)}\left(\frac{1}{4}-\alpha^2\right)|1+e^{j(\Delta\Phi_{at}+\Delta\phi_L)}|^2. \tag{19}$$

We repeat this calculation for initial positions on a three-dimensional grid to construct the image of the atomic cloud at the detection time t_{obs}. Subsequently, we integrate over the xy dimensions to obtain the total number of atoms at position z. To extract the atomic phase shift, we add a laser phase $\Delta\phi_L$ in Eq. (19) to probe the atomic phase and analyze the simulated images the exact same way we do with the experimental ones.

To evaluate the contribution of the mutual interaction we measured the interaction phase shift as a function of the condensate release time, the trapping frequency ν_z, and the population imbalance α. Figure 5 shows the variation of the phase gradient as a function of the release time T_F. We see that the phase gradient decreases with the release time and becomes almost undetectable after 20 ms. As expected,

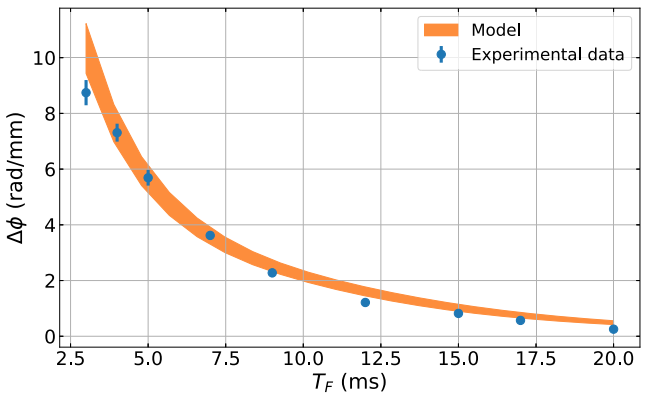

FIG. 5. Phase gradient as a function of the release time t_F. The orange shaded curve is the range of calculated phase gradient accounting for the uncertainty in the trapping frequencies.

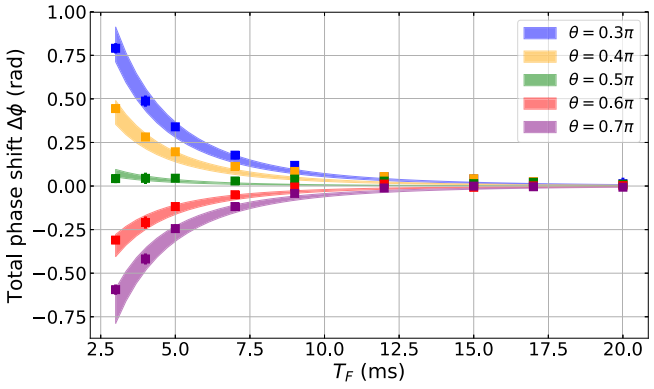

FIG. 6. Total phase shift accounting for both mutual and self-interactions as a function of the release time T_F for different values of the Raman pulse area θ (from 0.3π to 0.7π), with $T_R = 6$ ms. Squares show experimental data. The shaded curve is the range of calculated total interaction phase shift, accounting for uncertainty in the pulse area and the trapping frequencies.

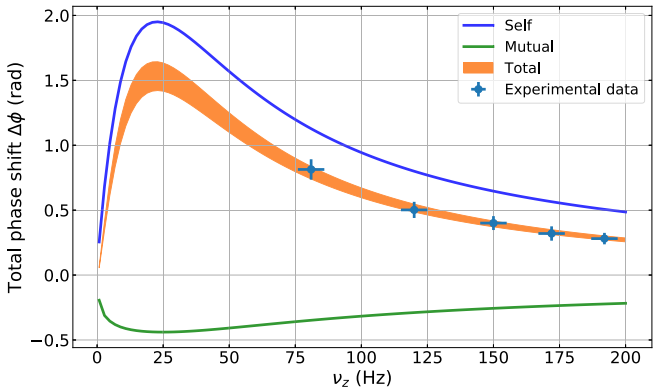

FIG. 7. Variation of the interaction phase shift with the vertical trapping frequency ν_z. Parameters are $T_F = 3$ ms, $T_R = 6$ ms, and $\theta = 0.35\ \pi$. The shaded orange curve is the range of calculated total interaction phase shift, accounting for uncertainty in the number of atoms and the trapping frequencies. The experimental data set satisfies the Thomas-Fermi approximation.

this is also the case for the total phase shift that accounts for both the mutual and self-interactions, even if the population imbalance between the two branches of the interferometer is significant (see Fig. 6). We measure a total interaction phase shift of 0.49 ± 0.03 rad for an atomic density in an initial BEC of 4.3×10^{14} atoms/cm^3 when $T_F = 4$ ms and $\theta = 0.3\ \pi$.

Finally, we looked at the behavior of the phase shift due to atomic interactions when varying the vertical trapping frequency ν_z. As shown in Fig. 7, the phase first increases with the trapping frequency, passes a maximum, and then decreases. This behavior results from the dependence of the chemical potential, BEC size, and expansion rate on trapping frequencies.

The mean field scales as $\bar{\omega}^{6/5}$; it increases faster than the size of the condensate, which varies almost linearly with the trapping frequency. Therefore, considering the overlap duration of the two condensates, the contribution of the self-interaction is larger than the mutual interaction.

For a low trapping frequency, the expansion of the atomic cloud is slow, and the two BECs rapidly separate after the first Raman pulse (with relative velocity $2v_r$). The main contribution to the total phase shift $\Delta\phi$ comes from the self-interaction, which increases rapidly as the trapping frequency increases. At a high trapping frequency, the expansion of the cloud dominates due to the repulsive potential, and therefore, the self-interaction decreases since both BECs are diluted.

IV. CONCLUSION

In this paper, we have investigated in detail both theoretically and experimentally the phase shift due to atomic interactions in an atom interferometer. Our theoretical model relies on the Feynman integral approach, which is used to derive general formulas for phase shifts related to self-interaction and mutual interaction. Our model is general and accounts for the effect of a population imbalance between the two arms of the interferometer as well as of the difference in scattering lengths of the hyperfine states. It allows us to evaluate precisely the interaction phase shifts knowing the time evolution of the spatial density of the Bose-Einstein condensate. Relying on the Castin-Dum model, which describes the temporal evolution of the BEC spatial density in the Thomas-Fermi regime, we calculated the phase shift induced by the atomic interactions and, in particular, the phase gradient resulting from the mutual interaction. We experimentally measured the phase gradient and the total phase shift (accounting for mutual and self-interactions) by varying the experimental parameters (BEC release time, trapping frequencies, and Raman coupling). The theoretical curves reproduce well the experimental data without any adjustment of the parameters. In particular, the work presented in this paper has enabled us to evaluate the phase gradient due to the mutual interactions between the two interfering condensates. It also provides theoretical tools, validated by the experiment, to evaluate the phase shifts induced by atomic interactions. The treatment of the interaction effect by the Feynman path-integral approach can be generalized to other atom-interferometer configurations and offers a simple way to accurately evaluate the related systematic effect that could affect high-precision measurements with atom interferometry.

ACKNOWLEDGMENTS

This work was supported by the Agence Nationale pour la Recherche TONICS Project-(Grant No. ANR-21-CE47-0017-01), the U.S. National Institute of Standards and Technology (NIST) Precision Measurement Grant Program under Award No. 60NANB16D271, and the LaBEx Cluster of Excellence FIRST-TF (Grant No. ANR-10-LABX-48-01), within the Programme investissements d'avenir operated by the French National Research Agency (ANR). C.S. acknowledges support from Region Ile-de-France through the DIM SIRTEQ Fellowship ELUDA.

[1] R. Geiger, A. Landragin, S. Merlet, and F. P. D. Santos, High-accuracy inertial measurements with cold-atom sensors, AVS Quantum Sci. **2**, 024702 (2020).

[2] Z.-K. Hu, B.-L. Sun, X.-C. Duan, M.-K. Zhou, L.-L. Chen, S. Zhan, Q.-Z. Zhang, and J. Luo, Demonstration of an ultrahigh-sensitivity atom-interferometry absolute gravimeter, Phys. Rev. A **88**, 043610 (2013).

[3] P. Gillot, O. Francis, A. Landragin, F. P. D. Santos, and S. Merlet, Stability comparison of two absolute gravimeters: Optical versus atomic interferometers, Metrologia **51**, L15 (2014).

[4] C. Freier, M. Hauth, V. Schkolnik, B. Leykauf, M. Schilling, H. Wziontek, H.-G. Scherneck, J. Müller, and A. Peters, Mobile quantum gravity sensor with unprecedented stability, J. Phys.: Conf. Ser. **723**, 012050 (2016).

[5] Y. Bidel, N. Zahzam, C. Blanchard, A. Bonnin, M. Cadoret, A. Bresson, D. Rouxel, and M. F. Lequentrec-Lalancette, Absolute marine gravimetry with matter-wave interferometry, Nat. Commun. **9**, 627 (2018).

[6] V. Ménoret, P. Vermeulen, N. L. Moigne, S. Bonvalot, P. Bouyer, A. Landragin, and B. Desruelle, Gravity measurements

below 10^{-9} g with a transportable absolute quantum gravimeter, Sci. Rep. **8**, 12300 (2018).

[7] Y. Bidel, N. Zahzam, A. Bresson, C. Blanchard, M. Cadoret, A. V. Olesen, and R. Forsberg, Absolute airborne gravimetry with a cold atom sensor, J. Geod. **94**, 20 (2020).

[8] D. Savoie, M. Altorio, B. Fang, L. A. Sidorenkov, R. Geiger, and A. Landragin, Interleaved atom interferometry for high-sensitivity inertial measurements, Sci. Adv. **4**, eaau7948 (2018).

[9] R. Gautier, M. Guessoum, L. A. Sidorenkov, Q. Bouton, A. Landragin, and R. Geiger, Accurate measurement of the Sagnac effect for matter waves, Sci. Adv. **8**, eabn8009 (2022).

[10] A. Bonnin, C. Diboune, N. Zahzam, Y. Bidel, M. Cadoret, and A. Bresson, New concepts of inertial measurements with multi-species atom interferometry, Appl. Phys. B **124**, 181 (2018).

[11] D. Yankelev, C. Avinadav, N. Davidson, and O. Firstenberg, Multiport atom interferometry for inertial sensing, Phys. Rev. A **100**, 023617 (2019).

[12] G. Rosi, F. Sorrentino, L. Cacciapuoti, M. Prevedelli, and G. M. Tino, Precision measurement of the Newtonian gravitational constant using cold atoms, Nature (London) **510**, 518 (2014).

[13] R. H. Parker, C. Yu, W. Zhong, B. Estey, and H. Müller, Measurement of the fine-structure constant as a test of the standard model, Science **360**, 191 (2018).

[14] L. Morel, Z. Yao, P. Cladé, and S. Guellati-Khélifa, Determination of the fine-structure constant with an accuracy of 81 parts per trillion, Nature (London) **588**, 61 (2020).

[15] G. M. Tino, Testing gravity with cold atom interferometry: Results and prospects, Quantum Sci. Technol. **6**, 024014 (2021).

[16] P. Asenbaum, C. Overstreet, M. Kim, J. Curti, and M. A. Kasevich, Atom-Interferometric Test of the Equivalence Principle at the 10^{-12} Level, Phys. Rev. Lett. **125**, 191101 (2020).

[17] H. Albers, A. Herbst, L. L. Richardson, H. Heine, D. Nath, J. Hartwig, C. Schubert, C. Vogt, M. Woltmann, C. LÃ¤mmerzahl, S. Herrmann, W. Ertmer, E. M. Rasel, and D. Schlippert, Quantum test of the universality of free fall using rubidium and potassium, Eur. Phys. J. D **74**, 145 (2020).

[18] B. Barrett, G. Condon, L. Chichet, L. Antoni-Micollier, R. Arguel, M. Rabault, C. Pelluet, V. Jarlaud, A. Landragin, P. Bouyer, and B. Battelier, Testing the universality of free fall using correlated ^{39}K–^{87}Rb atom interferometers, AVS Quantum Sci. **4**, 014401 (2022).

[19] S. Dimopoulos and A. A. Geraci, Probing submicron forces by interferometry of Bose-Einstein condensed atoms, Phys. Rev. D **68**, 124021 (2003).

[20] P. Wolf, P. Lemonde, A. Lambrecht, S. Bize, A. Landragin, and A. Clairon, From optical lattice clocks to the measurement of forces in the Casimir regime, Phys. Rev. A **75**, 063608 (2007).

[21] F. Sorrentino, A. Alberti, G. Ferrari, V. V. Ivanov, N. Poli, M. Schioppo, and G. M. Tino, Quantum sensor for atom-surface interactions below 10 μm, Phys. Rev. A **79**, 013409 (2009).

[22] X. Alauze, A. Bonnin, C. Solaro, and F. Pereira dos Santos, A trapped ultracold atom force sensor with a μm-scale spatial resolution, New J. Phys. **20**, 083014 (2018).

[23] P. Hamilton, M. Jaffe, P. Haslinger, Q. Simmons, H. Müller, and J. Khoury, Atom-interferometry constraints on dark energy, Science **349**, 849 (2015).

[24] K. Van Tilburg, N. Leefer, L. Bougas, and D. Budker, Search for Ultralight Scalar Dark Matter with Atomic Spectroscopy, Phys. Rev. Lett. **115**, 011802 (2015).

[25] B. Elder, J. Khoury, P. Haslinger, M. Jaffe, H. Müller, and P. Hamilton, Chameleon dark energy and atom interferometry, Phys. Rev. D **94**, 044051 (2016).

[26] P. W. Graham, D. E. Kaplan, J. Mardon, S. Rajendran, and W. A. Terrano, Dark matter direct detection with accelerometers, Phys. Rev. D **93**, 075029 (2016).

[27] P. W. Graham, D. E. Kaplan, J. Mardon, S. Rajendran, W. A. Terrano, L. Trahms, and T. Wilkason, Spin precession experiments for light axionic dark matter, Phys. Rev. D **97**, 055006 (2018).

[28] P. Haslinger, M. Jaffe, V. Xu, O. Schwartz, M. Sonnleitner, M. Ritsch-Marte, H. Ritsch, and H. Müller, Attractive force on atoms due to blackbody radiation, Nat. Phys. **14**, 257 (2018).

[29] D. O. Sabulsky, I. Dutta, E. A. Hinds, B. Elder, C. Burrage, and E. J. Copeland, Experiment to Detect Dark Energy Forces Using Atom Interferometry, Phys. Rev. Lett. **123**, 061102 (2019).

[30] K. Frye *et al.*, The Bose-Einstein condensate and cold atom laboratory, EPJ Quantum Technol. **8**, 1 (2021).

[31] D. N. Aguilera *et al.*, Ste-quest - test of the universality of free fall using cold atom interferometry, Class. Quantum Grav. **31**, 115010 (2014).

[32] D. Becker *et al.*, Space-borne Bose–Einstein condensation for precision interferometry, Nature (London) **562**, 391 (2018).

[33] P. Adamson, S. Chattopadhyay, J. Coleman, P. Graham, S. Geer, R. Harnik, S. Hahn, J. Hogan, M. Kasevich, T. Kovachy, J. Mitchell, R. Plunkett, S. Rajendran, L. Vaerio, and A. Vaspmos, Proposal: P-1101. Matter-wave atomic gradiometer interferometric sensor (magis-100), Fermi National Accelerator Lab.(FNAL), Batavia, IL (United States) (2018).

[34] A. Arvanitaki, P. W. Graham, J. M. Hogan, S. Rajendran, and K. Van Tilburg, Search for light scalar dark matter with atomic gravitational wave detectors, Phys. Rev. D **97**, 075020 (2018).

[35] B. Canuel *et al.*, Exploring gravity with the MIGA large scale atom interferometer, Sci. Rep. **8**, 14064 (2018).

[36] M.-S. Zhan *et al.*, Zaiga: Zhaoshan long-baseline atom interferometer gravitation antenna, Int. J. Mod. Phys. D **29**, 1940005 (2020).

[37] T. Lévèque, C. Fallet, M. Mandea, R. Biancale, J. M. Lemoine, S. Tardivel, S. Delavault, A. Piquereau, S. Bourgogne, F. P. dos Santos, B. Battelier, and P. Bouyer, Gravity field mapping using laser-coupled quantum accelerometers in space, J. Geod. **95**, 15 (2021).

[38] N. Zahzam, B. Christophe, V. Lebat, E. Hardy, P.-A. Huynh, N. Marquet, C. Blanchard, Y. Bidel, A. Bresson, P. Abrykosov, T. Gruber, R. Pail, I. Daras, and O. Carraz, Hybrid electrostatic-atomic accelerometer for future space gravity missions, Remote Sensing **14**, 3273 (2022).

[39] A. Louchet-Chauvet, T. Farah, Q. Bodart, A. Clairon, A. Landragin, S. Merlet, and F. Pereira dos Santos, The influence of transverse motion within an atomic gravimeter, New J. Phys. **13**, 065025 (2011).

[40] S. Bade, L. Djadaojee, M. Andia, P. Cladé, and S. Guellati-Khelifa, Observation of Extra Photon Recoil in a Distorted Optical Field, Phys. Rev. Lett. **121**, 073603 (2018).

[41] A. Wicht, E. Sarajlic, J. M. Hensley, and S. Chu, Phase shifts in precision atom interferometry due to the localization of atoms and optical fields, Phys. Rev. A **72**, 023602 (2005).

[42] P. Cladé, S. Guellati-Khélifa, F. Nez, and F. Biraben, Large Momentum Beam Splitter Using Bloch Oscillations, Phys. Rev. Lett. **102**, 240402 (2009).

[43] H. Müller, S.-W. Chiow, S. Herrmann, and S. Chu, Atom Interferometers with Scalable Enclosed Area, Phys. Rev. Lett. **102**, 240403 (2009).

[44] S.-W. Chiow, T. Kovachy, H.-C. Chien, and M. A. Kasevich, 102$\hbar k$ Large Area Atom Zinterferometers, Phys. Rev. Lett. **107**, 130403 (2011).

[45] M. Gebbe, J.-N. Siemß, M. Gersemann, H. Müntinga, S. Herrmann, C. Lämmerzahl, H. Ahlers, N. Gaaloul, C. Schubert, K. Hammerer, S. Abend, and E. M. Rasel, Twin-lattice atom interferometry, Nat. Commun. **12**, 2544 (2021).

[46] S. S. Szigeti, S. P. Nolan, J. D. Close, and S. A. Haine, High-Precision Quantum-Enhanced Gravimetry with a Bose-Einstein Condensate, Phys. Rev. Lett. **125**, 100402 (2020).

[47] B. K. Malia, J. Martínez-Rincón, Y. Wu, O. Hosten, and M. A. Kasevich, Free Space Ramsey Spectroscopy in Rubidium with Noise below the Quantum Projection Limit, Phys. Rev. Lett. **125**, 043202 (2020).

[48] M. A. Perlin, C. Qu, and A. M. Rey, Spin Squeezing with Short-Range Spin-Exchange Interactions, Phys. Rev. Lett. **125**, 223401 (2020).

[49] J. E. Simsarian, J. Denschlag, M. Edwards, C. W. Clark, L. Deng, E. W. Hagley, K. Helmerson, S. L. Rolston, and W. D. Phillips, Imaging the Phase of an Evolving Bose-Einstein Condensate Wave Function, Phys. Rev. Lett. **85**, 2040 (2000).

[50] A. O. Jamison, J. N. Kutz, and S. Gupta, Atomic interactions in precision interferometry using Bose-Einstein condensates, Phys. Rev. A **84**, 043643 (2011).

[51] A. O. Jamison, B. Plotkin-Swing, and S. Gupta, Advances in precision contrast interferometry with Yb Bose-Einstein condensates, Phys. Rev. A **90**, 063606 (2014).

[52] R. Jannin, P. Cladé, and S. Guellati-Khélifa, Phase shift due to atom-atom interactions in a light-pulse atom interferometer, Phys. Rev. A **92**, 013616 (2015).

[53] A. Burchianti, C. D'Errico, L. Marconi, F. Minardi, C. Fort, and M. Modugno, Effect of interactions in the interference pattern of Bose-Einstein condensates, Phys. Rev. A **102**, 043314 (2020).

[54] E. W. Hagley, L. Deng, M. Kozuma, M. Trippenbach, Y. B. Band, M. Edwards, M. Doery, P. S. Julienne, K. Helmerson, S. L. Rolston, and W. D. Phillips, Measurement of the Coherence of a Bose-Einstein Condensate, Phys. Rev. Lett. **83**, 3112 (1999).

[55] M. Trippenbach, Y. B. Band, M. Edwards, M. Doery, P. S. Julienne, E. W. Hagley, L. Deng, M. Kozuma, K. Helmerson, S. L. Rolston, and W. D. Phillips, Coherence properties of an atom laser, J. Phys. B **33**, 47 (2000).

[56] I. Bloch, T. W. Hänsch, and T. Esslinger, Measurement of the spatial coherence of a trapped Bose gas at the phase transition, Nature (London) **403**, 166 (2000).

[57] Y. Castin and R. Dum, Bose-Einstein Condensates in Time Dependent Traps, Phys. Rev. Lett. **77**, 5315 (1996).

[58] P. Storey and C. Cohen-Tannoudji, The Feynman path integral approach to atomic interferometry. A tutorial, J. Phys. II **4**, 1999 (1994).

[59] M. Cadoret, E. De Mirandes, P. Clade, F. Nez, L. Julien, F. Biraben, and S. Guellati-Khelifa, Atom interferometry based on light pulses: Application to the high precision measurement of the ratio h/m and the determination of the fine structure constant, Eur. Phys. J.: Spec. Top. **172**, 121 (2009).

[60] W. P. Schleich, D. M. Greenberger, and E. M. Rasel, A representation-free description of the Kasevich-Chu interferometer: A resolution of the redshift controversy, New J. Phys. **15**, 013007 (2013).

[61] A. Couvert, M. Jeppesen, T. Kawalec, G. Reinaudi, R. Mathevet, and D. Guéry-Odelin, A quasi-monomode guided atom laser from an all-optical Bose-Einstein condensate, Europhys. Lett. **83**, 50001 (2008).